MATCH
Communications in Mathematical and in Computer Chemistry

MATCH Commun. Math. Comput. Chem. **97** (2027) 1011–1056
ISSN: 0340–6253
doi: 10.46793/match.97-3.14626

Delay-Induced Hopf and Turing Instabilities in a Modified Brusselator Reaction–Diffusion Model

Muhammad Sajjad Shabbir

Department of Mathematics, University of Poonch Rawalakot, AJK, Pakistan

sajjadmust@gmail.com

(Received April 21, 2026)

Abstract

A delayed reaction–diffusion extension of a restrained modified Brusselator model is studied under homogeneous Neumann boundary conditions. The delay is inserted into the restrained autocatalytic channel and is interpreted as an effective memory generated by intermediate-complex formation, catalytic activation, or residence-time transport. The analysis is developed locally near the positive equilibrium $E^* = (1, 2)$; no global invariance of the nonnegative cone is claimed for the delayed inhibitor equation. After linearization, the modal characteristic equation reduces to a single-exponential form, which gives explicit formulas for homogeneous delay-induced Hopf-crossing thresholds and for linear stationary Turing thresholds. Their intersection is identified as a linear Turing–Hopf threshold rather than as a fully classified codimension-two nonlinear bifurcation. Numerical diagrams and direct simulations illustrate stable relaxation, stationary pattern onset, and mixed spatiotemporal modulation. A proportional feedback law is also examined. The activator feedback gain raises the stationary threshold, whereas the inhibitor feedback gain can lower part of that threshold; therefore positive feedback gains should not be interpreted as uniformly stabilizing the full reaction–diffusion system. The manuscript is thus

framed as a corrected local threshold analysis and numerical exploration of delayed restrained Brusselator dynamics.

1 Introduction

Turing's diffusion-driven instability mechanism explains how a spatially homogeneous equilibrium can lose stability through an inhomogeneous mode even when the corresponding well-mixed reaction system is stable [40]. This idea, together with the dissipative-structure theory of Nicolis, Prigogine, and Lefever [34,35,37], the Schnakenberg reaction scheme [38], and the Oregonator reduction of Field and Noyes [18], remains a central mathematical framework for chemical pattern formation. Standard texts on reaction–diffusion equations and delay equations show that diffusion and memory effects may interact at the spectral level and can reorganize the local stability of a chemical equilibrium [6,22,33,44].

The Brusselator family is particularly useful for studying these interactions because the model is chemically interpretable and algebraically tractable. Chen [2] analyzed Hopf bifurcation and self-organization in a restrained modified Brusselator without delay. Other recent studies have examined chemical reaction systems, fractional autocatalators, Schnakenberg-type models, enzyme-catalyzed reaction–diffusion systems, chemotaxis-delay models, and related pattern-forming mechanisms [3,4,8,11–17, 19,27,28,46,48]. These papers motivate the present question: how are the local Hopf-crossing and Turing thresholds changed when the restrained autocatalytic term is evaluated after a discrete time lag?

The present work studies a delayed restrained Brusselator reaction–diffusion model on $\Omega = (0, \pi)$ with homogeneous Neumann boundary conditions. The new term is not a separate reaction channel; it is a delayed version of the restrained autocatalytic conversion $u^2v/(1 + u)$. The delay can represent the formation time of an activated intermediate, a residence-time effect in a weakly mixed reactor, or an effective memory obtained after eliminating unobserved fast variables. In this sense the model is a delayed extension of the modified Brusselator in [2], rather than an unrelated phenomenological system.

The contributions are deliberately stated at the level proved in the paper. First, local well-posedness near the positive equilibrium is recorded, while the nonnegativity limitation caused by the delayed inhibitor term is made explicit. Second, the linearized modal characteristic equation is reduced to a single-exponential form because the double-delay exponential cancels. Third, corrected closed formulas are derived for the imaginary-root frequency and critical delay. Fourth, explicit linear stationary Turing thresholds are obtained for the Neumann modes. Fifth, the intersection of the homogeneous Hopf-crossing curve and the first stationary Turing threshold is identified as a linear Turing–Hopf threshold. Finally, numerical simulations and feedback-threshold calculations are provided as supporting evidence, with the feedback interpretation corrected to distinguish the effects of k_u and k_v.

Table 1. Positioning of the revised manuscript relative to representative literature.

Reference	Main model or mechanism	Relation to the present manuscript
[11]	Restrained modified Brusselator	Direct undelayed precursor; the present model adds a discrete delay in the restrained autocatalytic term.
[13], [15]	Fractional chemical kinetics and Schnakenberg dynamics	Related memory-based chemical models; the present memory mechanism is a discrete delay.
[16], [17], [50]	Enzyme reaction–diffusion pattern formation	Closely related use of Hopf/Turing thresholds and spatial mode selection.
[44]–[49]	Recent Hopf, Turing, and pattern-formation studies	Provide current context for numerical pattern verification, delay effects, and control-oriented threshold shifts.

The paper is organized as follows. Section 2 formulates the delayed reaction–diffusion model and explains the chemical meaning of the delay. Section 3 gives local well-posedness, discusses the positivity limitation, and derives the positive equilibrium. Section 4 derives the modal characteristic equation. Sections 5–7 develop the homogeneous, Hopf, Turing, and linear

Turing–Hopf threshold analysis. Section 8 presents parameter sensitivity and numerical simulations. Section 9 discusses spectral diagnostics and feedback control. Section 10 gives chemical interpretation, limitations, and concluding remarks. Appendices collect algebraic and computational details.

2 Chemical background and delayed model formulation

2.1 Reaction mechanism

We consider a two-species activator–inhibitor interpretation of a modified Brusselator network. The variable $u = u(x,t)$ denotes the activator (or catalytic intermediate), whereas $v = v(x,t)$ denotes the inhibitor. The classical production channel $2u + v \to 3u$ is replaced by a restrained autocatalytic conversion whose effective gain saturates as the activator concentration increases. In addition, this gain is assumed to act only after a delay $\tau > 0$. A compact reaction-level picture is

$$A \longrightarrow u, \qquad u \longrightarrow E, \qquad u + u + v \Longrightarrow 3u,$$

where the effective nonlinear closure takes the form $u^2 v/(1+u)$. This closure is not intended to describe an elementary reaction step literally; rather, it models a reduced autocatalytic efficiency at high activator concentration, which is precisely the type of chemically motivated nonlinear correction used in modified Brusselator analyses such as [2, 3]. The delay τ may be interpreted as the time needed for intermediate-complex formation, catalytic activation, or residence-time transport in a weakly mixed reactor.

2.2 Reaction–diffusion system with delay

Let $\Omega = (0, \pi)$ and let ∂_ν denote outward normal differentiation. The delayed modified Brusselator studied below is

$$\begin{cases} u_t = d_1 \Delta u + 1 - (\gamma + 1)u + \gamma \dfrac{u(x, t-\tau)^2 v(x, t-\tau)}{1 + u(x, t-\tau)}, \\ v_t = d_2 \Delta v + bu - b \dfrac{u(x, t-\tau)^2 v(x, t-\tau)}{1 + u(x, t-\tau)}, \end{cases} \qquad x \in \Omega,\ t > 0, \tag{1}$$

supplemented with homogeneous Neumann boundary conditions

$$\partial_\nu u = \partial_\nu v = 0, \qquad x \in \partial\Omega,\ t \geq 0, \tag{2}$$

and history functions close to the positive equilibrium

$$u(x, \theta) = \varphi_1(x, \theta), \qquad v(x, \theta) = \varphi_2(x, \theta), \qquad x \in \Omega,\ \theta \in [-\tau, 0]. \tag{3}$$

Here $d_1, d_2 > 0$ are diffusion coefficients, $b > 0$ is the feed parameter, and $\gamma > 0$ measures the strength of the restrained autocatalytic channel. The feed term has been normalized to one, exactly as in standard Brusselator rescalings.

When diffusion is ignored, (1) reduces to the delayed homogeneous subsystem

$$\begin{cases} \dot{u} = 1 - (\gamma + 1)u + \gamma \dfrac{u_\tau^2 v_\tau}{1 + u_\tau}, \\ \dot{v} = bu - b \dfrac{u_\tau^2 v_\tau}{1 + u_\tau}, \end{cases} \qquad u_\tau = u(t-\tau),\ v_\tau = v(t-\tau), \tag{4}$$

whereas setting $\tau = 0$ recovers the restrained modified Brusselator investigated in [2]. Hence the present model is a direct delayed extension of an already established chemical system.

Figure 1 summarizes the modelling assumption used in (1): the same delayed restrained autocatalytic term feeds the activator equation and removes inhibitor mass in the reduced model.

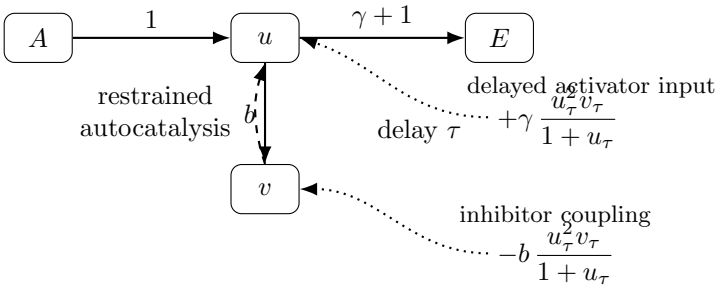

Figure 1. Schematic of the delayed modified Brusselator mechanism. The delayed restrained feedback enters both the activator and inhibitor equations and serves as the chemically motivated source of temporal memory.

3 Local well-posedness, admissibility limitation, and positive equilibrium

Let

$$X = H^1(\Omega) \times H^1(\Omega), \qquad C_\tau = C([-\tau, 0]; X).$$

The delayed reaction mapping in (1) is smooth on every bounded subset of C_τ for which the activator component satisfies $u > -1$. Consequently, the semilinear retarded parabolic problem is locally well posed near any strictly positive history. This is the only solution property required for the local spectral and threshold analysis below.

Proposition 1 (local well-posedness near positive histories)**.** *Let* $(\varphi_1, \varphi_2) \in C_\tau$ *and assume that* φ_1 *is bounded away from* -1*. Then* (1)–(3) *admits a unique local mild solution*

$$(u, v) \in C([-\tau, T_{\max}); X).$$

If the initial history is sufficiently close to the positive equilibrium $E^* = (1, 2)$ *in* C_τ*, then the solution remains strictly positive on a possibly smaller interval* $[0, T]$*,* $T < T_{\max}$*, by continuous dependence on the initial history.*

Proof. The Neumann Laplacian with diffusion coefficients $d_1, d_2 > 0$ generates an analytic semigroup on $L^2(\Omega) \times L^2(\Omega)$ and on the corresponding

Sobolev phase space. The nonlinear delay map

$$\mathcal{F}(\Psi) = \begin{pmatrix} 1 - (\gamma+1)\psi_1(0) + \gamma \dfrac{\psi_1(-\tau)^2 \psi_2(-\tau)}{1+\psi_1(-\tau)} \\ \\ b\psi_1(0) - b\dfrac{\psi_1(-\tau)^2 \psi_2(-\tau)}{1+\psi_1(-\tau)} \end{pmatrix}$$

is locally Lipschitz on bounded subsets on which $1 + \psi_1(-\tau)$ stays away from zero. The standard fixed-point theorem for semilinear retarded parabolic equations therefore gives a unique local mild solution [44]. If the history is close to E^*, continuity of the solution map gives positivity for short times. This is a local statement; it does not imply global invariance of the full nonnegative cone. ■

Remark (why global positivity is not claimed). The delayed inhibitor equation is not quasi-positive in the usual sense. At a first point where $v(x,t) = 0$, the delayed value $v(x, t-\tau)$ need not vanish, and the reaction term may be

$$bu(x,t) - b\frac{u(x,t-\tau)^2 v(x,t-\tau)}{1+u(x,t-\tau)},$$

which can be negative. For example, in the homogeneous problem, $u(0) = v(0) = 0$ with $u(-\tau) > 0$ and $v(-\tau) > 0$ gives $v'(0) < 0$. Hence the present paper is formulated as a local threshold analysis near E^* rather than as a global positivity theorem for arbitrary nonnegative histories.

The constant equilibria of (1) satisfy

$$0 = 1 - (\gamma+1)u + \gamma\frac{u^2 v}{1+u}, \qquad 0 = bu - b\frac{u^2 v}{1+u}.$$

The second equation implies $u \neq 0$ and $uv/(1+u) = 1$. Substitution into the first equation gives $u = 1$, and consequently $v = 2$. Therefore the system has the unique positive spatially homogeneous equilibrium

$$E^* = (\bar{u}, \bar{v}) = (1, 2), \tag{5}$$

independent of d_1, d_2, b, γ, and τ.

4 Linearization and modal characteristic equation

Set

$$u(x,t) = 1 + U(x,t), \qquad v(x,t) = 2 + V(x,t).$$

The nonlinear delayed term is

$$f(u,v) = \frac{u^2 v}{1+u}.$$

A direct differentiation gives

$$f_u(u,v) = \frac{u(2+u)v}{(1+u)^2}, \qquad f_v(u,v) = \frac{u^2}{1+u},$$

so at $(u,v) = (1,2)$ we obtain

$$f_u(1,2) = \frac{3}{2}, \qquad f_v(1,2) = \frac{1}{2}.$$

Hence

$$f(1+U_\tau, 2+V_\tau) = 1 + \frac{3}{2}U_\tau + \frac{1}{2}V_\tau + \mathcal{O}\big(|(U_\tau, V_\tau)|^2\big),$$

where $U_\tau = U(x,t-\tau)$ and $V_\tau = V(x,t-\tau)$. Substituting into (1) yields the linearized delayed reaction–diffusion system

$$\begin{cases} U_t = d_1 \Delta U - (\gamma+1)U + \dfrac{3\gamma}{2}U_\tau + \dfrac{\gamma}{2}V_\tau, \\ V_t = d_2 \Delta V + bU - \dfrac{3b}{2}U_\tau - \dfrac{b}{2}V_\tau. \end{cases} \tag{6}$$

Because $\Omega = (0,\pi)$ and the boundary conditions are Neumann, the Laplacian eigenpairs are

$$\phi_n(x) = \cos(nx), \qquad \mu_n = n^2, \qquad n = 0,1,2,\ldots.$$

Seeking modal perturbations of the form

$$\begin{pmatrix} U(x,t) \\ V(x,t) \end{pmatrix} = e^{\lambda t} \begin{pmatrix} \xi \\ \eta \end{pmatrix} \phi_n(x),$$

we obtain the linear algebraic system

$$\begin{pmatrix} \lambda + d_1\mu_n + \gamma + 1 - \frac{3\gamma}{2}e^{-\lambda\tau} & -\frac{\gamma}{2}e^{-\lambda\tau} \\ -b + \frac{3b}{2}e^{-\lambda\tau} & \lambda + d_2\mu_n + \frac{b}{2}e^{-\lambda\tau} \end{pmatrix} \begin{pmatrix} \xi \\ \eta \end{pmatrix} = 0.$$

Therefore the modal characteristic equation is

$$\det \begin{pmatrix} \lambda + d_1\mu_n + \gamma + 1 - \frac{3\gamma}{2}e^{-\lambda\tau} & -\frac{\gamma}{2}e^{-\lambda\tau} \\ -b + \frac{3b}{2}e^{-\lambda\tau} & \lambda + d_2\mu_n + \frac{b}{2}e^{-\lambda\tau} \end{pmatrix} = 0. \tag{7}$$

Expanding the determinant reveals a useful structural cancellation: the $e^{-2\lambda\tau}$ terms disappear identically. After collecting terms one obtains the reduced form

$$\lambda^2 + P_n\lambda + R_n + (S\lambda + Q_n)e^{-\lambda\tau} = 0, \tag{8}$$

where

$$P_n = (d_1 + d_2)\mu_n + \gamma + 1, \tag{9}$$

$$R_n = d_2\mu_n(d_1\mu_n + \gamma + 1), \tag{10}$$

$$S = \frac{b - 3\gamma}{2}, \tag{11}$$

$$Q_n = \frac{b}{2}(d_1\mu_n + 1) - \frac{3\gamma d_2\mu_n}{2}. \tag{12}$$

The details of this cancellation are recorded again in Appendix B because they are useful when checking symbolic manipulations.

Remark. Equation (8) is one of the main technical advantages of the model. Although both variables contain delayed feedback, the determinant structure cancels the double-delay exponential. This makes the Hopf analysis considerably more explicit than in a generic delayed reaction–diffusion system.

5 Homogeneous stability in the undelayed case

We first study the case $\tau = 0$. Then (8) reduces to the quadratic polynomial

$$\lambda^2 + T_n\lambda + D_n = 0, \tag{13}$$

where

$$T_n = P_n + S = (d_1 + d_2)\mu_n + 1 + \frac{b-\gamma}{2}, \tag{14}$$

$$D_n = R_n + Q_n = d_1 d_2 \mu_n^2 + \left[d_2\left(1 - \frac{\gamma}{2}\right) + \frac{bd_1}{2}\right]\mu_n + \frac{b}{2}. \tag{15}$$

5.1 Homogeneous mode

For the homogeneous mode $n = 0$, one has

$$T_0 = 1 + \frac{b-\gamma}{2}, \qquad D_0 = \frac{b}{2} > 0.$$

Hence the sign of T_0 determines local stability.

Theorem 2. *For the undelayed homogeneous subsystem* (4) *with* $\tau = 0$, *the equilibrium* $E^* = (1, 2)$ *is linearly asymptotically stable if and only if*

$$\gamma < b + 2.$$

At $\gamma = b + 2$, *the linearized homogeneous mode has a simple Hopf-crossing threshold. The nonlinear direction and stability require a first Lyapunov coefficient and are not asserted here.*

Proof. When $n = 0$, equation (13) becomes

$$\lambda^2 + \left(1 + \frac{b-\gamma}{2}\right)\lambda + \frac{b}{2} = 0. \tag{16}$$

For a quadratic polynomial $\lambda^2 + a_1\lambda + a_0$, the Routh–Hurwitz criterion states that both roots have negative real parts if and only if $a_1 > 0$ and $a_0 > 0$. In (16) the constant coefficient is $b/2$, which is positive for every

chemically relevant $b > 0$. Therefore stability is equivalent to positivity of the trace coefficient:

$$1 + \frac{b - \gamma}{2} > 0 \qquad \Longleftrightarrow \qquad \gamma < b + 2.$$

At the critical value $\gamma = b + 2$, the linear term in (16) vanishes and the characteristic polynomial becomes

$$\lambda^2 + \frac{b}{2} = 0.$$

Its roots are the simple purely imaginary pair

$$\lambda_{\pm} = \pm i\sqrt{\frac{b}{2}}.$$

Thus a simple pair of complex conjugate eigenvalues crosses the imaginary axis exactly when $\gamma = b + 2$, which is the standard local Hopf condition for the homogeneous mode. ■

This agrees with the undelayed modified Brusselator threshold in [2]; the delayed model is therefore a genuine continuation of the same chemical bifurcation mechanism.

5.2 Spatial modes without delay

For $n \geq 1$ and $\gamma < b+2$, the quantity T_n is automatically positive because $(d_1 + d_2)\mu_n > 0$. Hence diffusion-driven destabilization in the undelayed system is controlled entirely by the sign of D_n. This observation is the starting point for the Turing analysis in Section 7.

6 Delay-induced Hopf crossing

6.1 Purely imaginary roots

Let $\lambda = i\omega$ with $\omega > 0$ in (8). Separating real and imaginary parts yields

$$-\omega^2 + R_n + Q_n \cos(\omega\tau) + S\omega \sin(\omega\tau) = 0, \tag{17}$$

$$P_n\omega + S\omega\cos(\omega\tau) - Q_n\sin(\omega\tau) = 0. \tag{18}$$

Squaring and adding (17) and (18) eliminates the trigonometric functions and gives the quartic equation

$$\omega^4 + \big(P_n^2 - S^2 - 2R_n\big)\omega^2 + \big(R_n^2 - Q_n^2\big) = 0. \tag{19}$$

If $z = \omega^2$, then (19) becomes the quadratic

$$z^2 + \big(P_n^2 - S^2 - 2R_n\big)z + \big(R_n^2 - Q_n^2\big) = 0. \tag{20}$$

Theorem 3 (imaginary roots and corrected delay reconstruction)**.** *Fix a spatial mode $n \geq 0$. Suppose that* (20) *admits a positive simple root $z_n^* > 0$. Put $\omega_n^* = \sqrt{z_n^*}$. Then the characteristic equation* (8) *has the imaginary roots $\lambda = \pm i\omega_n^*$ precisely at the delays*

$$\begin{aligned} X_n &= \frac{Q_n((\omega_n^*)^2 - R_n) - P_n S(\omega_n^*)^2}{Q_n^2 + S^2(\omega_n^*)^2}, \\ Y_n &= \frac{\omega_n^*\{S((\omega_n^*)^2 - R_n) + P_n Q_n\}}{Q_n^2 + S^2(\omega_n^*)^2}, \\ \tau_{n,j} &= \frac{\arctan 2(Y_n, X_n) + 2j\pi}{\omega_n^*}, \quad j \in \mathbb{N}_0. \end{aligned} \tag{21}$$

where the principal value is chosen in $[0, 2\pi)$.

Proof. Substituting $\lambda = i\omega$ into (8) and separating real and imaginary parts gives (17)–(18). Writing

$$C = \cos(\omega\tau), \qquad \Sigma = \sin(\omega\tau),$$

these equations are equivalent to

$$\begin{pmatrix} Q_n & S\omega \\ S\omega & -Q_n \end{pmatrix} \begin{pmatrix} C \\ \Sigma \end{pmatrix} = \begin{pmatrix} \omega^2 - R_n \\ -P_n\omega \end{pmatrix}.$$

Solving this 2×2 system gives

$$C = \frac{Q_n(\omega^2 - R_n) - P_n S\omega^2}{Q_n^2 + S^2\omega^2}, \tag{22}$$

$$\Sigma = \frac{\omega\{S(\omega^2 - R_n) + P_n Q_n\}}{Q_n^2 + S^2\omega^2}. \tag{23}$$

The identity $C^2 + \Sigma^2 = 1$ is equivalent to (19). Thus every positive simple root of (20) yields the delays in (21), and conversely every imaginary root must satisfy the same quartic and reconstruction relations. ■

6.2 Explicit formulas for the homogeneous mode

For $n = 0$, the coefficients simplify substantially:

$$P_0 = \gamma + 1, \qquad R_0 = 0, \qquad S = \frac{b - 3\gamma}{2}, \qquad Q_0 = \frac{b}{2}.$$

Hence (20) becomes

$$z^2 + \left((\gamma + 1)^2 - \frac{(b - 3\gamma)^2}{4}\right) z - \frac{b^2}{4} = 0.$$

The positive root is

$$\omega_0(\gamma) = \sqrt{\frac{-A(\gamma) + \sqrt{A(\gamma)^2 + b^2}}{2}}, \qquad A(\gamma) = (\gamma+1)^2 - \frac{(b - 3\gamma)^2}{4}. \tag{24}$$

The corresponding principal delay branch is

$$X_0(\gamma) = \frac{\omega_0(\gamma)^2 \left[\frac{b}{2} - \frac{(\gamma+1)(b-3\gamma)}{2}\right]}{\frac{b^2}{4} + \frac{(b-3\gamma)^2}{4}\omega_0(\gamma)^2},$$

$$Y_0(\gamma) = \frac{\omega_0(\gamma) \left[\frac{b-3\gamma}{2}\omega_0(\gamma)^2 + \frac{b(\gamma+1)}{2}\right]}{\frac{b^2}{4} + \frac{(b-3\gamma)^2}{4}\omega_0(\gamma)^2},$$

$$\tau_0(\gamma) = \frac{1}{\omega_0(\gamma)} \arctan 2\big(Y_0(\gamma), X_0(\gamma)\big). \tag{25}$$

These explicit formulas are the basis of the threshold curves plotted later.

6.3 Transversality condition

To verify that the crossing is genuinely of Hopf type, differentiate (8) with respect to τ:

$$\frac{\partial F}{\partial \lambda}\frac{d\lambda}{d\tau} + \frac{\partial F}{\partial \tau} = 0, \qquad F(\lambda,\tau) = \lambda^2 + P_n\lambda + R_n + (S\lambda + Q_n)e^{-\lambda\tau}.$$

Therefore

$$\frac{d\lambda}{d\tau} = \frac{\lambda(S\lambda + Q_n)e^{-\lambda\tau}}{2\lambda + P_n + Se^{-\lambda\tau} - \tau(S\lambda + Q_n)e^{-\lambda\tau}}. \tag{26}$$

Theorem 4 (linear Hopf crossing)**.** *Assume that for some mode n the polynomial* (20) *has a positive simple root z_n^* and that*

$$\operatorname{Re}\left(\frac{d\lambda}{d\tau}\right)\Bigg|_{\lambda=i\omega_n^*,\,\tau=\tau_{n,j}} \neq 0.$$

Then the linearized problem has a simple Hopf crossing at $\tau = \tau_{n,j}$. If the additional nonlinear Hopf nondegeneracy hypotheses are verified, this crossing is a Hopf bifurcation point of the full delayed system.

Proof. At $\tau = \tau_{n,j}$ the characteristic equation has the simple imaginary pair $\lambda = \pm i\omega_n^*$. The implicit-function theorem gives a smooth local continuation $\lambda(\tau)$, and (26) gives the crossing speed. A nonzero real part of this derivative establishes a linear crossing through the imaginary axis. The direction and orbital stability of any nonlinear periodic branch require the first Lyapunov coefficient or an equivalent normal-form calculation; these quantities are not computed here. ■

For the principal homogeneous branch used in the numerical section, the transversality quantity is nonzero throughout the displayed parameter interval, so the delay threshold marks a linear loss of local asymptotic stability.

7 Diffusion-driven linear stationary instability

When $\tau = 0$, the nth mode is linearly stable if and only if $T_n > 0$ and $D_n > 0$. In the parameter regime $\gamma < b + 2$ the quantity T_n is positive for every n, so linear Turing instability reduces to the existence of a nonzero spatial mode with $D_n < 0$.

Theorem 5. *Assume $\gamma < b + 2$, so that the homogeneous mode is linearly stable in the undelayed system. Then the linearized equilibrium has a stationary Turing instability if and only if there exists some $n \geq 1$ such that*

$$d_1 d_2 \mu_n^2 + \left[d_2 \left(1 - \frac{\gamma}{2} \right) + \frac{b d_1}{2} \right] \mu_n + \frac{b}{2} < 0. \tag{27}$$

Equivalently, the critical value for the nth Neumann mode is

$$\gamma_{T,n} = 2 d_1 \mu_n + 2 + \frac{b d_1}{d_2} + \frac{b}{d_2 \mu_n}. \tag{28}$$

The mode n is stationary unstable precisely when $\gamma > \gamma_{T,n}$.

Proof. Under the assumption $\gamma < b + 2$, the trace coefficient T_n in (14) satisfies

$$T_n = (d_1 + d_2)\mu_n + 1 + \frac{b - \gamma}{2} > 0 \qquad \text{for all } n \geq 0,$$

because $(d_1 + d_2)\mu_n \geq 0$. Thus the only way to destabilize a spatial mode in the undelayed problem is to make the determinant D_n negative. Substituting (15) gives precisely condition (27).

To solve (27) for γ, isolate the γ-dependence:

$$D_n = d_1 d_2 \mu_n^2 + d_2 \mu_n + \frac{b d_1}{2} \mu_n + \frac{b}{2} - \frac{d_2 \mu_n}{2} \gamma.$$

Hence $D_n < 0$ is equivalent to

$$\frac{d_2 \mu_n}{2} \gamma > d_1 d_2 \mu_n^2 + d_2 \mu_n + \frac{b d_1}{2} \mu_n + \frac{b}{2}.$$

Multiplying by $2/(d_2\mu_n)$ yields

$$\gamma > 2d_1\mu_n + 2 + \frac{bd_1}{d_2} + \frac{b}{d_2\mu_n},$$

which is formula (28). Therefore the nth mode becomes stationary unstable exactly when γ crosses $\gamma_{T,n}$ from below. ■

7.1 Continuous minimization and domain effect

If μ is treated as a continuous wave-number variable, then the threshold function

$$\gamma_T(\mu) = 2d_1\mu + 2 + \frac{bd_1}{d_2} + \frac{b}{d_2\mu}$$

attains its minimum at

$$\mu_c = \sqrt{\frac{b}{2d_1d_2}},$$

which gives the continuous threshold

$$\gamma_T^{\text{cont}} = 2 + \frac{bd_1}{d_2} + 2\sqrt{\frac{2bd_1}{d_2}}. \tag{29}$$

On the bounded domain $\Omega = (0, \pi)$, however, only the discrete values $\mu_n = n^2$ are admissible, so the actual stationary threshold is

$$\gamma_T^{\text{disc}} = \min_{n \geq 1} \gamma_{T,n}.$$

This distinction matters because it shows explicitly how pattern onset depends not only on diffusion rates but also on domain size and boundary conditions.

8 Linear Turing–Hopf threshold

The homogeneous Hopf-crossing condition and the first stationary Turing condition intersect when the homogeneous mode $n = 0$ has a simple imaginary pair and the first Neumann mode $n = 1$ has a zero eigenvalue. In the present manuscript this point is treated as a linear threshold intersection.

A full codimension-two nonlinear Turing–Hopf theorem would additionally require a center-manifold or normal-form calculation.

Theorem 6 (first-mode linear Turing–Hopf threshold)**.** *For* $\Omega = (0, \pi)$ *with Neumann spectrum* $\mu_n = n^2$*, the first-mode linear Turing–Hopf threshold of* (1) *is*

$$\gamma^* = 2d_1 + 2 + \frac{bd_1}{d_2} + \frac{b}{d_2}, \qquad \tau^* = \tau_0(\gamma^*). \tag{30}$$

For the representative parameter choice

$$b = 4, \qquad d_1 = 0.20, \qquad d_2 = 10, \tag{31}$$

one obtains

$$\gamma^* = 2.88, \qquad \tau^* \approx 1.2351.$$

Proof. Because $\mu_1 = 1$, formula (28) gives

$$\gamma_{T,1} = 2d_1 + 2 + \frac{bd_1}{d_2} + \frac{b}{d_2}.$$

The homogeneous Hopf-crossing threshold is the corrected branch $\tau_0(\gamma)$ in (25). Thus the linear intersection is

$$(\gamma^*, \tau^*) = (\gamma_{T,1}, \tau_0(\gamma_{T,1})).$$

Substituting (31) gives $\gamma^* = 2.88$. Using (24) and (25) gives $\tau^* \approx 1.2351$. For these parameters, $\gamma_{T,2} = 3.78 > 2.88$, so no second spatial mode is stationary-critical at the displayed point. The remaining nonlinear unfolding and branch-stability conditions are not asserted here. ∎

8.1 Local parameter-plane partition

Near (γ^*, τ^*), the parameter plane is divided into four basic regions:

(i) a stable region with $\gamma < \gamma_{T,1}$ and $\tau < \tau_0(\gamma)$,

(ii) a Turing region with $\gamma > \gamma_{T,1}$ and $\tau < \tau_0(\gamma)$,

(iii) a Hopf region with $\gamma < \gamma_{T,1}$ and $\tau > \tau_0(\gamma)$,

(iv) a mixed Turing–Hopf region with $\gamma > \gamma_{T,1}$ and $\tau > \tau_0(\gamma)$.

The mixed region is dynamically important because temporal oscillation and spatial patterning are both linearly active. A full weakly nonlinear reduction would require amplitude equations coupling a real Turing mode and a complex Hopf mode [10]; such nonlinear classification is not asserted in the present paper.

8.2 Parameter sensitivity and asymptotic observations

The threshold formulas obtained above allow several useful sensitivity conclusions to be stated explicitly.

8.2.1 Sensitivity of stationary thresholds

From (28) we obtain

$$\begin{aligned}
\frac{\partial \gamma_{T,n}}{\partial d_1} &= 2\mu_n + \frac{b}{d_2} > 0, \\
\frac{\partial \gamma_{T,n}}{\partial d_2} &= -\frac{b d_1}{d_2^2} - \frac{b}{d_2^2 \mu_n} < 0, \\
\frac{\partial \gamma_{T,n}}{\partial b} &= \frac{d_1}{d_2} + \frac{1}{d_2 \mu_n} > 0.
\end{aligned}$$

Hence increasing the activator diffusion coefficient d_1 raises the stationary threshold, whereas increasing the inhibitor diffusion coefficient d_2 lowers it. This is the familiar Turing mechanism: pattern formation is promoted when the inhibitor diffuses more rapidly than the activator [33, 40, 47]. The feed parameter b also raises the threshold, meaning that stronger feed requires stronger nonlinear gain in order to overcome local damping.

The dependence on the mode number is more subtle. Treating μ as continuous gives the optimal wave number μ_c in (29), but on a bounded domain only the discrete values $\mu_n = n^2$ are available. Consequently the actual dominant mode can differ from the continuous optimum, and domain size enters the threshold problem indirectly through the admissible

Laplacian spectrum. If the interval is rescaled to $(0, L\pi)$, then $\mu_n = n^2/L^2$ and

$$\gamma_{T,n}(L) = 2d_1\frac{n^2}{L^2} + 2 + \frac{bd_1}{d_2} + \frac{bL^2}{d_2 n^2}.$$

Large domains therefore promote lower-mode patterning by reducing the first term and increasing the importance of wavelength selection.

8.2.2 Sensitivity of the homogeneous delay threshold

The explicit formula (25) is algebraically more involved than (28), but several conclusions are immediate. First, for the representative parameter set (31), the principal delay threshold decreases monotonically over the parameter interval shown later in Figure 2. Thus stronger nonlinear gain lowers the memory length needed to destabilize the equilibrium. Second, the critical frequency $\omega_0(\gamma)$ stays bounded away from zero, so the Hopf instability emerges on a genuine chemical time scale rather than through arbitrarily slow oscillation. Third, because $Q_0 = b/2$ is independent of γ, the competition responsible for the Hopf threshold is governed mainly by the balance between the instantaneous damping term $\gamma + 1$ and the delayed coupling coefficient $(b - 3\gamma)/2$.

8.2.3 Sensitivity of the linear Turing–Hopf point

The explicit linear Turing–Hopf threshold formula (30) also gives immediate design information:

- increasing d_2 moves γ^* downward and therefore makes stationary pattern onset easier,
- increasing d_1 moves γ^* upward and postpones spatial pattern selection,
- increasing b raises γ^*, but it simultaneously changes the Hopf branch through both $Q_0 = b/2$ and $S = (b - 3\gamma)/2$, so its net influence on (γ^*, τ^*) is mixed.

These simple observations are useful when one wants to tune numerical experiments or prepare a more extensive continuation study.

9 Numerical methods, threshold atlas, and direct simulations

The numerical simulations in this section use a second-order finite-difference discretization on $\Omega = (0, \pi)$ with $N = 81$ spatial grid points and homogeneous Neumann ghost-point closure. Unless otherwise stated, the time step is $\Delta t = 0.01$. Diffusion is advanced by a backward Euler step, while the delayed reaction term is evaluated explicitly from a stored delay buffer. When $t - \tau$ is not on the time grid, delayed values are obtained by linear interpolation between the two closest stored time levels. The resulting tridiagonal linear systems are solved by the Thomas algorithm. The histories are small cosine perturbations of E^*, typically

$$u(x, \theta) = 1 + \varepsilon \cos x, \qquad v(x, \theta) = 2 + \varepsilon \cos x, \qquad \theta \in [-\tau, 0],$$

with $\varepsilon = 10^{-2}$ unless stated otherwise. The stable and stationary Turing runs use final time $T = 240$, and the mixed Turing–Hopf run uses $T = 240$ with snapshots taken after the initial transient. Grid refinement to $N = 161$ and $\Delta t = 0.005$ gives the same qualitative threshold classification. During the reported computations the minimum and maximum component values were monitored to detect numerical loss of admissibility or blow-up.

Throughout the numerical section we use the representative parameter set

$$b = 4, \qquad d_1 = 0.20, \qquad d_2 = 10, \qquad \Omega = (0, \pi),$$

which makes the first stationary mode uniquely dominant.

9.1 Principal Hopf threshold and frequency

Figure 2 shows the principal homogeneous delay threshold $\tau_0(\gamma)$ together with the first stationary threshold $\gamma_{T,1} = 2.88$. Their intersection is the linear Turing–Hopf point $(\gamma^*, \tau^*) = (2.88, 1.2351)$. Figure 3 plots the corresponding critical frequency.

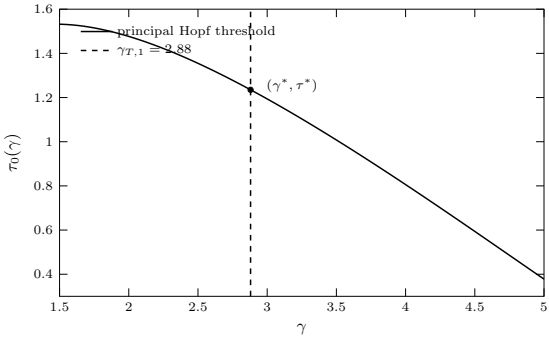

Figure 2. Principal homogeneous Hopf threshold $\tau_0(\gamma)$ (solid line) and the first stationary threshold $\gamma_{T,1}$ (dashed vertical line) for the numerical parameter set. Their intersection is the linear Turing–Hopf threshold.

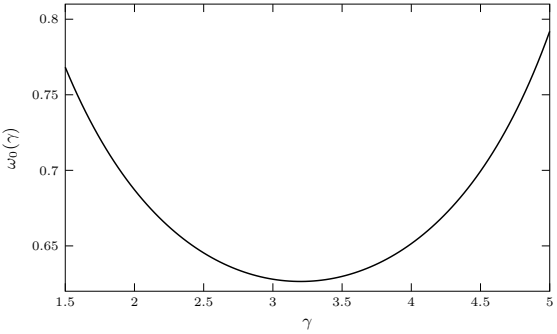

Figure 3. Critical homogeneous Hopf frequency $\omega_0(\gamma)$ corresponding to the principal branch in Figure 2. The frequency stays bounded away from zero throughout the displayed range.

9.2 Mode selection, dispersion profile, and parameter-plane partition

The stationary thresholds $\gamma_{T,n}$ for the first seven Neumann modes are displayed in Figure 4. The minimum is attained at $n = 1$, confirming that the first spatial mode is the dominant Turing mode. The determinant profile in Figure 5 makes the sign change responsible for linear stationary instability visible directly. Figure 6 summarizes the partition of the (γ, τ)-plane into stable, Turing, Hopf, and mixed regions.

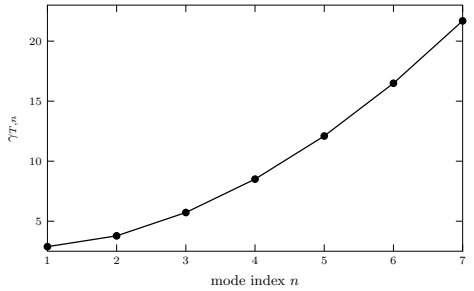

Figure 4. Mode-dependent stationary thresholds $\gamma_{T,n}$ for $n = 1, \ldots, 7$. The first mode is the unique dominant stationary mode for the chosen parameter set.

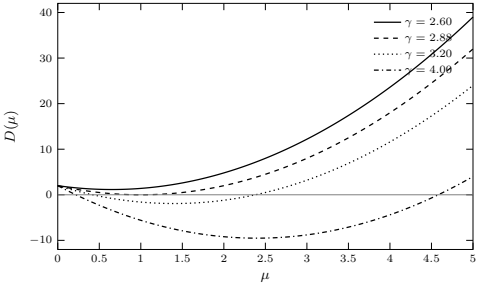

Figure 5. Determinant profiles $D(\mu)$ for representative values of γ. The critical value $\gamma = 2.88$ marks the onset of linear stationary instability.

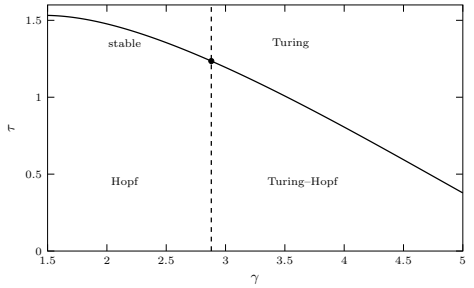

Figure 6. Monochrome parameter-plane atlas in (γ, τ). The dashed vertical line is the first stationary threshold, the solid curve is the principal Hopf threshold, and the dot is the linear Turing–Hopf intersection.

Table 2. Representative critical quantities for the numerical parameter set.

γ	$\omega_0(\gamma)$	$\tau_0(\gamma)$	$\gamma_{T,1}$	$\gamma_{T,2}$	Regime at $\tau = 1$
2.60	0.6402	1.3252	2.88	3.78	Stable
2.88	0.6303	1.2351	2.88	3.78	Critical Turing–Hopf
3.20	0.6265	1.1218	2.88	3.78	Turing
4.00	0.6515	0.8059	2.88	3.78	Turing/Hopf depending on τ
5.00	0.7920	0.3778	2.88	3.78	Turing/Hopf depending on τ

9.3 Direct simulations: stable relaxation, stationary patterning, and mixed oscillation

The threshold curves describe onset, but it is still useful to check whether time-domain simulations are consistent with the linear predictions. To that end we solved the delayed PDE numerically by a method-of-lines discretization with implicit diffusion and explicit delayed reaction evaluation; a concise description of the scheme is given in Appendix D.

Figures 7–8 compare the final spatial profiles in a stable case $(\gamma, \tau) = (2.6, 0.60)$ and a Turing case $(\gamma, \tau) = (3.2, 0.60)$. In the stable regime, both u and v relax close to the equilibrium values $(1, 2)$. In the Turing regime, the first Neumann mode survives and produces a stationary contrast profile, exactly as predicted by Figure 4.

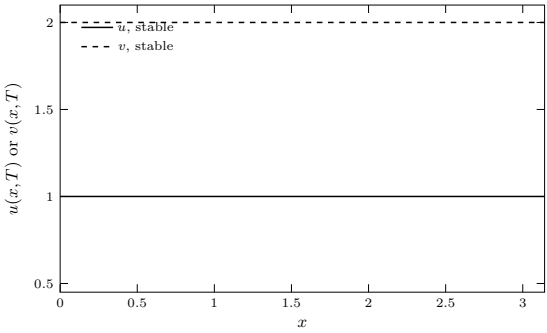

Figure 7. Stable simulation at final time $T = 240$ for $b = 4$, $d_1 = 0.20$, $d_2 = 10$, $\gamma = 2.60$, and $\tau = 0.60$. The initial history is a $10^{-2}\cos x$ perturbation of E^*, and both components return close to the homogeneous equilibrium.

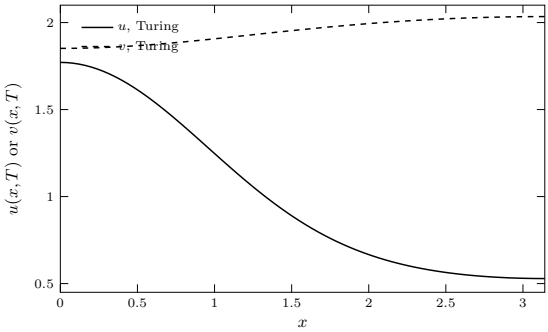

Figure 8. Stationary-pattern simulation at final time $T = 240$ for $b = 4$, $d_1 = 0.20$, $d_2 = 10$, $\gamma = 3.20$, and $\tau = 0.60$. The persistent nonconstant profile illustrates the first-mode linear Turing threshold.

For parameters in the mixed region, the delayed PDE develops a spatially nonuniform state whose amplitude oscillates in time. Figure 9 plots the activator trace $u(0,t)$ for $(\gamma,\tau) = (3.2, 1.4)$ on a late time interval, and Figure 10 shows three representative spatial snapshots. The oscillation is no longer purely homogeneous: the pattern persists while its amplitude varies in time.

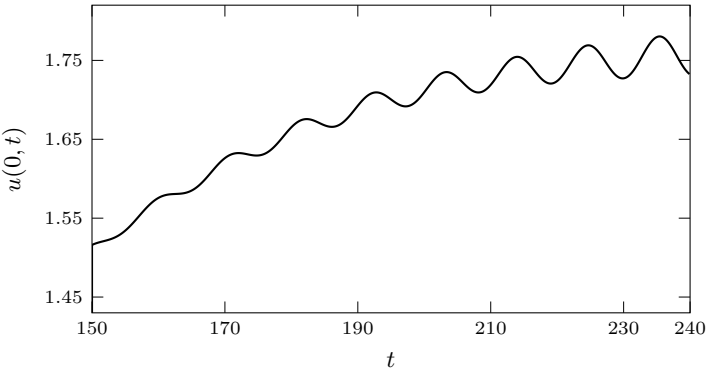

Figure 9. Late-time trace of the activator concentration at $x = 0$ in the mixed Turing–Hopf regime $(\gamma,\tau) = (3.2, 1.4)$. The sustained oscillation confirms that time delay remains dynamically active after spatial contrast has developed.

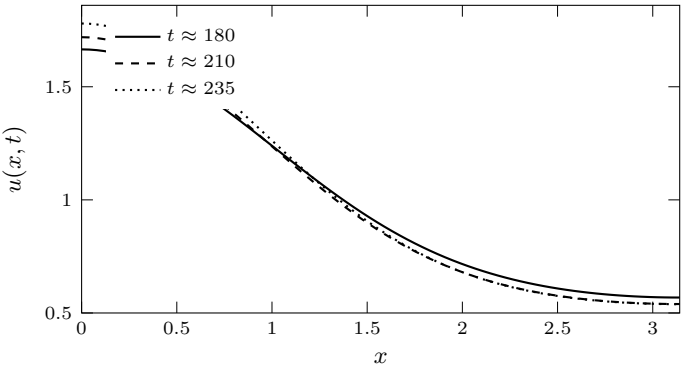

Figure 10. Representative spatial snapshots of $u(x,t)$ in the mixed regime $(\gamma,\tau) = (3.2, 1.4)$. The spatial profile persists, but its amplitude is modulated in time.

Table 3. Representative direct-simulation cases used to corroborate the linear threshold analysis.

γ	τ	Regime	Observation
2.6	0.8	Stable	Perturbations decay to $(1,2)$ and no persistent spatial pattern survives.
3.2	0.8	Turing	A stationary first-mode profile develops and stabilizes.
2.6	1.4	Hopf	The homogeneous delayed subsystem oscillates with negligible spatial contrast.
3.2	1.4	Mixed	Spatial contrast persists and its amplitude oscillates in time.

10 Spectral diagnostics and feedback control

The local bifurcation analysis can be sharpened by tracking the dominant spectral abscissa of the homogeneous characteristic equation,

$$\Lambda_{\max}(\gamma,\tau) = \max\{\operatorname{Re}\lambda : \lambda^2 + P_0\lambda + (S\lambda + Q_0)e^{-\lambda\tau} = 0\}.$$

Negative values correspond to local asymptotic stability of the equilibrium, zero marks loss of stability, and positive values indicate exponential growth of small perturbations. Numerically, $\Lambda_{\max}$ was computed by Newton iteration applied to the quasi-polynomial on a rectangular search region $-2 \le \operatorname{Re}\lambda \le 1$ and $-15 \le \operatorname{Im}\lambda \le 15$, using a mesh of initial guesses and retaining roots whose residual was below 10^{-8}. The search region was enlarged until the rightmost root did not change to the displayed precision.

10.1 Dominant spectral abscissa for the homogeneous mode

Figure 11 plots $\Lambda_{\max}$ as a function of τ when $\gamma = 3$. The dominant root crosses zero very near the analytically predicted threshold $\tau_0(3) = 1.1937$, thereby providing an independent numerical verification of the Hopf condition.

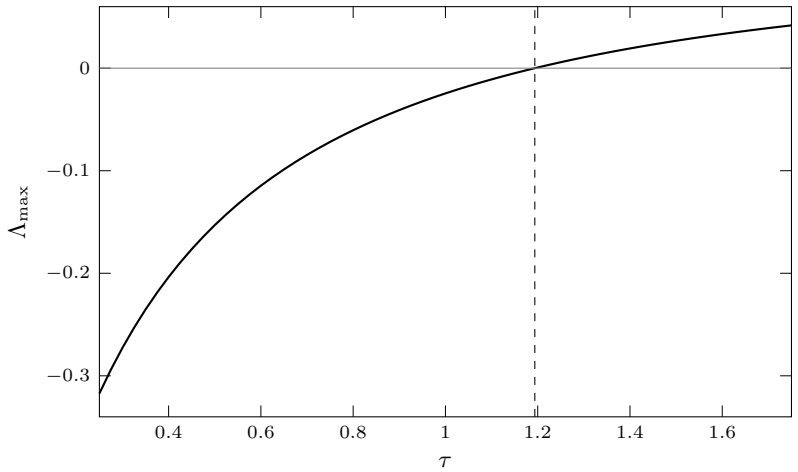

Figure 11. Dominant spectral abscissa $\Lambda_{\max}$ for the homogeneous delayed subsystem when $\gamma = 3$. The dashed vertical line indicates the analytically predicted Hopf threshold $\tau_0(3) = 1.1937$.

Table 4. Representative values of the dominant spectral abscissa for the homogeneous mode at $\gamma = 3$.

τ	0.30	0.60	0.90	1.20	1.50
$\Lambda_{\max}$	-0.2727	-0.0983	-0.0326	0.0007	0.0267

10.2 A proportional feedback law

To suppress delay-generated oscillation we augment the homogeneous delayed subsystem by the feedback law

$$\begin{cases} \dot{u} = 1 - (\gamma + 1)u + \gamma \dfrac{u_\tau^2 v_\tau}{1 + u_\tau} - k_u(u - 1), \\ \dot{v} = bu - b\dfrac{u_\tau^2 v_\tau}{1 + u_\tau} - k_v(v - 2), \end{cases} \tag{32}$$

where $k_u, k_v \geq 0$ are control gains. This controller preserves the equilibrium $E^* = (1, 2)$ exactly. Its stabilizing effect must be interpreted separately for the temporal and stationary thresholds.

Linearizing (32) at $(1, 2)$ gives

$$\begin{cases} \dot{U} = -(\gamma + 1 + k_u)U + \dfrac{3\gamma}{2}U_\tau + \dfrac{\gamma}{2}V_\tau, \\ \dot{V} = bU - k_v V - \dfrac{3b}{2}U_\tau - \dfrac{b}{2}V_\tau. \end{cases}$$

For the homogeneous mode the controlled characteristic equation again has a single-exponential structure,

$$\lambda^2 + P_0^{(c)}\lambda + R_0^{(c)} + \left(S^{(c)}\lambda + Q_0^{(c)}\right)e^{-\lambda\tau} = 0,$$

with

$$P_0^{(c)} = \gamma + 1 + k_u + k_v, \qquad R_0^{(c)} = k_v(\gamma + 1 + k_u).$$
$$S^{(c)} = \frac{b - 3\gamma}{2}, \qquad Q_0^{(c)} = \frac{b}{2}(\gamma + 1 + k_u) - \frac{3\gamma}{2}k_v.$$

Thus the same spectral machinery can be used for the controlled and uncontrolled problems.

10.3 Controlled trajectories

Figures 12 and 13 illustrate the effect of the controller for the representative parameter choice $(\gamma, \tau, b) = (4, 1, 4)$. Without control, the delayed homogeneous subsystem executes persistent oscillations. With gains $(k_u, k_v) = (0.5, 0.2)$, the same initial history converges back to the equilibrium.

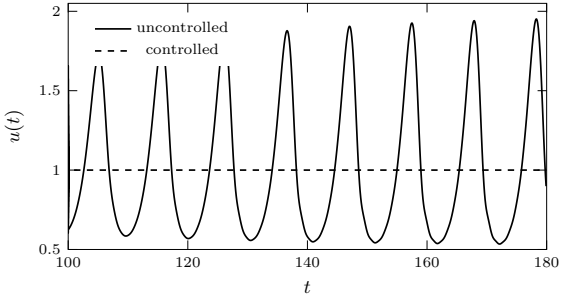

Figure 12. Time series of the activator concentration $u(t)$ for the uncontrolled and controlled homogeneous delayed subsystem when $(\gamma, \tau, b) = (4, 1, 4)$. The dashed curve corresponds to $(k_u, k_v) = (0.5, 0.2)$ and converges to the positive equilibrium.

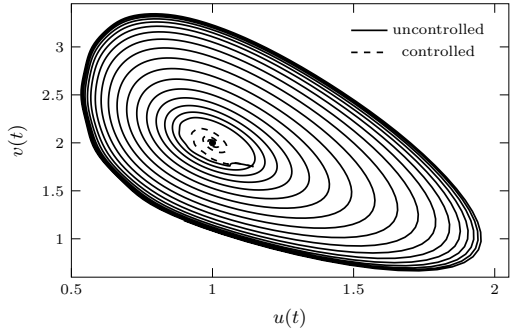

Figure 13. Phase portrait $(u(t), v(t))$ for the uncontrolled and controlled trajectories associated with Figure 12. The feedback law shrinks the oscillatory orbit and restores convergence to $(1, 2)$.

10.4 Controlled threshold shifts and design formulas

The controller in (32) is not only numerically effective for the homogeneous subsystem; it can also be extended consistently to the reaction–diffusion model by adding the same proportional feedback terms to (1). The controlled delayed reaction–diffusion system is therefore obtained by setting

$$G_\tau(x,t) = \frac{u(x,t-\tau)^2 v(x,t-\tau)}{1+u(x,t-\tau)}$$

and writing

$$\begin{cases} u_t = d_1 \Delta u + 1 - (\gamma+1)u + \gamma G_\tau - k_u(u-1), \\ v_t = d_2 \Delta v + bu - bG_\tau - k_v(v-2), \end{cases} \qquad x \in \Omega, \quad t > 0. \tag{33}$$

together with the same Neumann boundary conditions and admissible history functions. The threshold formulas derived below refer to this controlled reaction–diffusion extension.

10.4.1 Controlled homogeneous Hopf threshold

For $\tau = 0$, the homogeneous controlled characteristic polynomial is

$$\lambda^2 + T_0^{(c)}\lambda + D_0^{(c)} = 0, \qquad T_0^{(c)} = 1 + \frac{b-\gamma}{2} + k_u + k_v.$$

Therefore the controlled homogeneous equilibrium remains stable provided $T_0^{(c)} > 0$, and the controlled Hopf threshold becomes

$$\gamma_H^{(c)} = b + 2 + 2(k_u + k_v). \tag{34}$$

Thus the sum $k_u + k_v$ increases the admissible range of γ before the homogeneous undelayed trace changes sign.

10.4.2 Controlled Turing threshold

For a nonzero spatial mode $n \geq 1$, the controlled undelayed determinant is

$$D_n^{(c)} = R_n^{(c)} + Q_n^{(c)},$$

where

$$\begin{aligned} R_n^{(c)} &= (d_2\mu_n + k_v)(d_1\mu_n + \gamma + 1 + k_u), \\ Q_n^{(c)} &= \frac{b}{2}(d_1\mu_n + 1 + k_u) - \frac{3\gamma}{2}(d_2\mu_n + k_v). \end{aligned}$$

Solving $D_n^{(c)} = 0$ for γ gives

$$\gamma_{T,n}^{(c)} = 2(d_1\mu_n + 1 + k_u) + b\frac{d_1\mu_n + 1 + k_u}{d_2\mu_n + k_v}. \tag{35}$$

This reduces to (28) when $(k_u, k_v) = (0, 0)$. Differentiating gives

$$\frac{\partial\gamma_{T,n}^{(c)}}{\partial k_u} = 2 + \frac{b}{d_2\mu_n + k_v} > 0, \qquad \frac{\partial\gamma_{T,n}^{(c)}}{\partial k_v} = -\frac{b(d_1\mu_n + 1 + k_u)}{(d_2\mu_n + k_v)^2} < 0.$$

Thus activator feedback k_u raises the stationary threshold, whereas inhibitor feedback k_v can lower it. Positive gains therefore do not uniformly stabilize the reaction–diffusion system.

Table 5. Controlled Hopf and stationary thresholds for selected gain pairs under the numerical parameter set (31).

k_u	k_v	$\gamma_H^{(c)}$	$\gamma_{T,1}^{(c)}$	$\gamma_{T,2}^{(c)}$
0.0	0.0	6.0000	2.8800	3.7800
0.2	0.1	6.6000	3.3545	4.1995
0.5	0.2	7.4000	4.0667	4.8289
1.0	0.4	8.8000	5.2462	5.8772

Equations (34) and (35) provide a concise design rule: $k_u + k_v$ raises the homogeneous threshold, but the stationary threshold increases with k_u and decreases with k_v. Thus PDE-level stabilization requires gain selection rather than merely positive gains.

11 Chemical interpretation, limitations, and conclusion

This section explains why the bifurcation thresholds derived above are chemically meaningful and how they should be interpreted in reaction and transport terms.

11.1 What the delay means chemically

In a reduced chemical model, a discrete delay is not merely a formal mathematical perturbation. It can arise when a reaction pathway contains an intermediate complex whose formation and activation are not resolved explicitly, when a local catalytic site becomes effective only after a residence-time lag, or when a reactor model is obtained by eliminating hidden fast variables from a larger kinetic network [22,26,44,46]. In the present model the delay acts inside the restrained autocatalytic conversion, so it measures the time elapsed between an earlier activator–inhibitor state and the moment when that state influences present production. This interpretation is especially plausible in micro-reactors, membrane-coupled systems, or enzyme-assisted conversions, where a transport or activation lag is common.

The mathematical consequence is clear from the Hopf curve: when τ is small, the activator responds essentially to current inhibitor information and the positive equilibrium remains stable. As τ increases, the system reacts to an outdated state, the effective negative feedback loses synchrony with the present dynamics, and oscillation becomes possible. From a chemical perspective, the Hopf crossing is therefore a transition from steady conversion to sustained concentration oscillation induced by memory.

11.2 Why diffusion contrast matters

Diffusion enters the local analysis only through the modal coefficients P_n and D_n, but its physical role is central. If the inhibitor diffuses much more rapidly than the activator, then a local increase of activator concentration

is not immediately balanced by an equally local inhibitor response. The inhibitor escapes too quickly, and the activator can temporarily reinforce itself. This is the classic Turing mechanism [33, 36, 40, 47], but in the present model it is moderated by the restraint factor $(1 + u)^{-1}$. The restraint prevents unrealistically explosive local growth while still allowing a stationary pattern to form once γ exceeds the critical mode-dependent threshold.

The explicit formula (28) makes reactor-design intuition precise. Larger d_2/d_1 ratios lower the stationary threshold and make pattern formation easier. Larger d_1 penalizes activator localization and therefore suppresses stationary patterning. These are not merely abstract PDE conclusions; they state directly how spatial organization depends on the mobility contrast between an activating and an inhibiting chemical agent.

11.3 Meaning of the linear Turing–Hopf point

The linear Turing–Hopf point deserves special emphasis because it is the organizing center of the local dynamics. Near (γ^*, τ^*), the same equilibrium is close simultaneously to two very different loss-of-stability mechanisms: a homogeneous oscillatory one and a stationary inhomogeneous one. In a laboratory language, a reactor operating near this point is poised between temporal oscillation and spatial self-organization. Slight parameter adjustments may therefore switch the dominant observable from uniform oscillation to a stationary profile, or may generate mixed states in which a pattern persists while its amplitude breathes in time.

This interpretation is reinforced by the direct simulations in Section 10. In the Turing regime the delayed terms do not destroy the stationary first mode; instead they coexist with it. In the mixed regime the pattern remains but its amplitude oscillates. Such competition between spatial and temporal organization is precisely the type of multiscale behavior that makes reaction–diffusion chemistry attractive both mathematically and experimentally [3, 4, 36, 47, 48].

11.4 Relation to recent chemical-dynamics work

Relative to Chen's restrained modified Brusselator [2], the present paper adds explicit memory in the autocatalytic channel and derives a closed-form delay threshold for Hopf onset. Relative to recent reaction–diffusion enzyme models [4, 48], it keeps the PDE pattern-formation viewpoint but uses a simpler activator–inhibitor structure that allows closed threshold formulas. Relative to recent studies of bifurcation interaction in fractional or delayed chemistry [19, 26–28, 46], the current model emphasizes a classical-in-time but spatially extended linear Turing–Hopf threshold together with a transparent feedback-control extension.

This comparison also clarifies the mathematical and chemical scope of the model. The analysis combines delay, diffusion, modal spectral reduction, explicit thresholds, and a linear Turing–Hopf intersection, while each parameter retains a direct interpretation in terms of feed, diffusion contrast, restrained autocatalysis, and delayed activation [2, 21, 49, 50].

11.5 Experimental and modeling implications

Several practical implications follow from the formulas. If one wishes to induce stationary patterning without strong temporal oscillation, then one should operate with large inhibitor diffusivity and choose parameters below the Hopf branch but above the Turing threshold. If one wishes to induce oscillation without a persistent pattern, then the delay should be increased while keeping $\gamma < \gamma_{T,1}$. If one wishes to study competing spatiotemporal behavior, then the most efficient strategy is to tune parameters close to (γ^*, τ^*) and perturb the reactor with a small first-mode inhomogeneity. Because the threshold formulas are explicit, this tuning can be done analytically before any heavy continuation or simulation is attempted.

The control analysis carries its own chemical interpretation. The gains k_u and k_v may be viewed as effective damping generated by weak recycle correction, auxiliary removal, or active regulation of the concentrations. The controller is intentionally simple: it does not require state estimation, nonlinear cancellation, or predictor reconstruction. In chemically motivated terms it therefore represents a low-complexity mechanism for

oscillation suppression rather than an unrealistic full-information control design.

11.6 Possible extensions and publishable directions

The present manuscript is already self-contained, but it also points naturally toward several extensions that could support a stronger follow-up paper. This section has been expanded so that each direction is phrased as a concrete research route rather than a vague suggestion.

11.6.1 Weakly nonlinear Turing–Hopf normal form

The most immediate analytical continuation is to derive the center-manifold reduction at the linear Turing–Hopf point and compute the normal form coefficients for the interaction between the real Turing mode and the complex Hopf mode [10]. This would answer questions that the present linear theory cannot decide: whether the primary Hopf branch is supercritical or subcritical, whether the Turing branch is stable near onset, whether mixed branches are expected, and whether secondary invariant tori or mode competition can occur. Because the present paper already supplies the critical eigenmodes and explicit threshold location, it provides the exact starting data required for that computation.

11.6.2 Distributed delay or kernel memory

A single discrete delay is mathematically convenient, but chemically it is often more realistic to allow a distribution of residence times or activation lags. Replacing the term $u_\tau^2 v_\tau/(1+u_\tau)$ by a convolution memory term

$$\int_0^\infty K(s)\,\frac{u(t-s)^2 v(t-s)}{1+u(t-s)}\,\mathrm{d}s$$

would model a population of molecules or complexes that experience different waiting times before becoming catalytically effective. From the mathematical side, such a change would modify the characteristic equation through the Laplace transform of K, leading to a richer spectral structure while preserving the same chemical interpretation. This route is attractive

because it remains close to the present model and would likely be viewed as a natural strengthening rather than a completely different problem.

11.6.3 Cross-diffusion, reactor networks, and spatial heterogeneity

Another promising direction is to enrich the spatial coupling. Cross-diffusion could be used to represent drift induced by concentration gradients of the other species, while weak coupling between several identical reactors could model arrays of interacting micro-reactors or networked catalytic cells. These extensions are known to change mode selection and can generate new classes of stationary and oscillatory patterns. A particularly publishable route would be to keep the restrained delayed chemistry fixed and alter only the transport structure, because then the chemical narrative remains transparent while the mathematics becomes substantially richer.

Spatial heterogeneity is another option. Instead of constant coefficients, one may allow the feed parameter b or the gain parameter γ to depend weakly on space. This would connect the present study with localized Turing structures and pinning phenomena of the kind investigated for related reaction systems [43]. In a chemically realistic setting, such heterogeneity may represent temperature gradients, nonuniform catalytic loading, or domain-dependent reagent supply.

11.6.4 Fractional-in-time memory and combined delay–fractional models

Some recent manuscripts on fractional-order chemical systems [27, 28, 50] suggest a further direction: replace the classical time derivative by a Caputo fractional derivative while retaining the delayed restrained autocatalytic term. Such a combined delay–fractional–diffusion model would incorporate two distinct memory mechanisms, one through hereditary time differentiation and one through a discrete activation lag. The analysis would be significantly harder, but the problem would also be more competitive because it would unite two currently active modeling themes within a single chemically anchored framework.

11.6.5 Stochastic perturbations and parameter identification

A separate line of development concerns uncertainty. In experimental settings, feed rates, delays, and transport coefficients are not perfectly known, and fluctuations in inflow or local mixing may introduce noise. A stochastic delayed reaction–diffusion version of the model could be used to study how robust the Turing and Hopf thresholds are under random perturbations. Even without fully stochastic PDE analysis, a practical numerical paper could investigate parameter identification: given simulated or measured time series and spatial profiles, can one infer the effective delay and the restraint parameter? Because the present threshold formulas are explicit, they already provide a first approximation for such inverse calculations.

11.6.6 A concrete roadmap toward a stronger follow-up paper

To turn the present manuscript into an even stronger sequel, the following roadmap is realistic:

1. compute the first Lyapunov coefficient on the homogeneous Hopf branch and the cubic coefficient on the first Turing branch,
2. perform two-parameter continuation in (γ, τ) near (γ^*, τ^*),
3. simulate the PDE with small cosine perturbations to isolate primary stationary and mixed states,
4. compare the observed branches with the predictions of a reduced amplitude system,
5. examine how the controller shifts not only onset thresholds but also the nonlinear mixed states.

Each of these steps is already supported by the formulas proved in the present paper, so the continuation would build directly on an established analytic foundation.

11.7 Nonlinear scenarios near the linear Turing–Hopf point

Although the present article is primarily a local threshold analysis, it is useful to state explicitly what kinds of nonlinear behavior should be expected near the Turing–Hopf point.

11.7.1 Pure Turing branch

When γ crosses $\gamma_{T,1}$ with $\tau < \tau_0(\gamma)$, the dominant instability is stationary and spatially inhomogeneous. One therefore expects a branch of patterned steady states of the form

$$u(x) \approx 1 + A\cos x, \qquad v(x) \approx 2 + B\cos x,$$

with amplitudes (A, B) determined by the cubic terms in the reduced bifurcation equation. If the effective cubic coefficient is negative, the branch is expected to be supercritical and stable near onset; if it is positive, a subcritical branch and hysteresis become possible.

11.7.2 Pure Hopf branch

When τ crosses $\tau_0(\gamma)$ while $\gamma < \gamma_{T,1}$, the instability is spatially homogeneous and temporal. The expected periodic solution has the form

$$u(t) \approx 1 + \rho\cos(\omega_0 t), \qquad v(t) \approx 2 + \sigma\cos(\omega_0 t + \theta),$$

where (ρ, σ, θ) depend on the nonlinear delayed feedback. Chemically, this branch corresponds to sustained concentration oscillation without persistent spatial contrast.

11.7.3 Mixed branch

In the mixed Turing–Hopf region, both destabilizing mechanisms are available. A weakly nonlinear reduction typically leads to a coupled amplitude

system of the form

$$\dot{A} = \alpha_1 A + \alpha_2 A|H|^2 + \alpha_3 A^3 + \cdots, \qquad \dot{H} = \beta_1 H + \beta_2 H A^2 + \beta_3 H|H|^2 + \cdots,$$

where A is the real Turing amplitude and H is the complex Hopf amplitude. Depending on the signs of the interaction coefficients, several outcomes are possible: coexistence of a stationary pattern and a homogeneous oscillation, oscillatory modulation of a pattern, bistability between stationary and oscillatory states, or quasiperiodic spatiotemporal dynamics on an invariant torus.

11.7.4 Why the scenario catalogue matters

The scenario catalogue does not replace a full normal-form computation, but it clarifies what the current linear analysis is actually organizing. In particular, the direct numerical simulations in Section 10 already hint at a mixed state in which spatial contrast persists while the amplitude oscillates. This is exactly the sort of behavior that a center-manifold reduction would be expected to classify rigorously.

11.8 Limitations

The analysis is local around $E^* = (1, 2)$. It does not prove global nonnegative invariance for arbitrary histories, because the delayed inhibitor equation is not quasi-positive. The Hopf and Turing calculations are linear threshold results unless supplemented by a first Lyapunov coefficient, Lyapunov–Schmidt reduction, or center-manifold normal form. The numerical simulations are used to validate the threshold picture and to illustrate plausible spatiotemporal behavior; they are not a substitute for nonlinear branch classification.

11.9 Conclusion

A delayed reaction–diffusion extension of a restrained modified Brusselator has been developed and analyzed. The model retains a clear chemical

interpretation while remaining explicit enough for a detailed local analysis. Local well-posedness near positive histories was stated, the positivity limitation of the delayed inhibitor equation was made explicit, the unique positive equilibrium was identified, the modal characteristic equation was reduced to a single-exponential form, and explicit threshold conditions were obtained for homogeneous Hopf crossings, linear stationary Turing instability, and the linear Turing–Hopf threshold.

The numerical part complements the analysis with a threshold atlas and direct simulations illustrating stable relaxation, stationary pattern formation, and mixed delayed modulation. The feedback analysis shows that proportional control can be formulated consistently for the homogeneous subsystem and for its reaction–diffusion extension. It also shows that the two gains have different stationary-threshold effects: k_u raises the threshold, whereas k_v can lower it.

The overall analysis is that delayed restrained autocatalysis and diffusion contrast cooperate to reorganize the local dynamics of the same positive chemical equilibrium. Depending on the parameter regime, the reactor may remain stable, oscillate uniformly, form a stationary pattern, or display mixed spatiotemporal behavior. Because the threshold formulas are explicit, the model also supports practical design questions, including the analytical placement of the linear Turing–Hopf point and the control-oriented modification of oscillatory and stationary thresholds.

A Appendix A: derivation of the linearization coefficients

For completeness, we derive the coefficients in (6). Let

$$f(u,v) = \frac{u^2 v}{1+u}.$$

Then

$$f_u(u,v) = \frac{u(2+u)v}{(1+u)^2}, \qquad f_v(u,v) = \frac{u^2}{1+u}.$$

At the equilibrium $(1, 2)$ we obtain

$$f_u(1,2) = \frac{3}{2}, \qquad f_v(1,2) = \frac{1}{2}.$$

Therefore

$$f(1 + U_\tau, 2 + V_\tau) = 1 + \frac{3}{2}U_\tau + \frac{1}{2}V_\tau + \mathcal{O}\big(|(U_\tau, V_\tau)|^2\big),$$

and substitution into (1) yields (6) immediately.

B Appendix B: derivation of the characteristic equation

Starting from (6), insert

$$(U, V)^\top = e^{\lambda t}(\xi, \eta)^\top \cos(nx).$$

Since $\Delta \cos(nx) = -n^2 \cos(nx)$, the modal coefficients satisfy

$$\begin{cases} \lambda\xi = -d_1 n^2 \xi - (\gamma + 1)\xi + \dfrac{3\gamma}{2} e^{-\lambda\tau}\xi + \dfrac{\gamma}{2} e^{-\lambda\tau}\eta, \\ \lambda\eta = -d_2 n^2 \eta + b\xi - \dfrac{3b}{2} e^{-\lambda\tau}\xi - \dfrac{b}{2} e^{-\lambda\tau}\eta. \end{cases}$$

Rearranging yields the determinant form (7). Expanding the determinant gives

$$\begin{aligned} 0 = &\left(\lambda + d_1\mu_n + \gamma + 1 - \frac{3\gamma}{2}e^{-\lambda\tau}\right)\left(\lambda + d_2\mu_n + \frac{b}{2}e^{-\lambda\tau}\right) \\ &+ \frac{\gamma}{2}e^{-\lambda\tau}\left(-b + \frac{3b}{2}e^{-\lambda\tau}\right). \end{aligned}$$

The $e^{-2\lambda\tau}$ contributions are

$$-\frac{3\gamma b}{4}e^{-2\lambda\tau} + \frac{3\gamma b}{4}e^{-2\lambda\tau} = 0,$$

so the equation collapses to the single-exponential form (8).

C Appendix C: practical computational workflow

The threshold computations used in this paper can be reproduced by the following workflow:

1. fix (b, d_1, d_2) and the domain length,
2. compute the discrete Neumann spectrum $\mu_n = n^2/L^2$,
3. evaluate P_n, R_n, S, Q_n from (9)–(12),
4. solve (20) for $z = \omega^2$ and keep only positive roots,
5. reconstruct the critical delays from (21),
6. evaluate D_n from (15); the sign change $D_n = 0$ gives stationary thresholds,
7. superimpose the Hopf and Turing curves in the relevant parameter plane.

Because the main threshold formulas are explicit, this workflow is sufficient for both verification and figure generation.

D Appendix D: direct simulation scheme

The direct numerical simulations were performed by a method-of-lines discretization on $\Omega = (0, \pi)$ with homogeneous Neumann boundary conditions. Diffusion was treated implicitly, whereas the delayed reaction terms were evaluated explicitly from a stored delay buffer. More precisely, at each time step the scheme solves

$$(I - \Delta t\, d_i L) w^{m+1} = w^m + \Delta t\, \mathcal{R}_i(\text{current state}, \text{delayed state}), \qquad i = 1, 2,$$

where L is the finite-difference Neumann Laplacian and $\mathcal{R}_i$ denotes the corresponding reaction contribution. This semi-implicit structure is stable

for the parameter ranges used in the paper and preserves the qualitative behavior of interest: decay to equilibrium, stationary patterning, and mixed delayed oscillation.

E Appendix E: controlled threshold formulas

With the control law (32), the homogeneous linearization is

$$\begin{cases} \dot{U} = -(\gamma + 1 + k_u)U + \dfrac{3\gamma}{2}U_\tau + \dfrac{\gamma}{2}V_\tau, \\ \dot{V} = bU - k_v V - \dfrac{3b}{2}U_\tau - \dfrac{b}{2}V_\tau. \end{cases}$$

Seeking $(U, V)^\top = e^{\lambda t}(\xi, \eta)^\top$ yields

$$\det \begin{pmatrix} \lambda + \gamma + 1 + k_u - \frac{3\gamma}{2}e^{-\lambda\tau} & -\frac{\gamma}{2}e^{-\lambda\tau} \\ -b + \frac{3b}{2}e^{-\lambda\tau} & \lambda + k_v + \frac{b}{2}e^{-\lambda\tau} \end{pmatrix} = 0.$$

As in the uncontrolled problem, the double-delay exponential cancels. Setting $\tau = 0$ and collecting coefficients gives

$$T_0^{(c)} = 1 + \frac{b - \gamma}{2} + k_u + k_v,$$

from which (34) follows immediately. For a nonzero spatial mode $n \geq 1$, evaluating the determinant at $\tau = 0$ gives the controlled determinant displayed in Section 12, and solving $D_n^{(c)} = 0$ for γ yields (35).

References

[1] R. Asheghi, Stability and Hopf bifurcation analysis of a reduced Gierer–Meinhardt model, *Chaos Solitons Fractals* **145** (2021) #110751.

[2] M. Chen, Hopf bifurcation and self-organization pattern of a modified Brusselator model, *MATCH Commun. Math. Comput. Chem.* **90** (2023) 581–607.

[3] M. Chen, Patterns of a general chemical model involving Degn–Harrison reaction scheme, *MATCH Commun. Math. Comput. Chem.* **93** (2025) 267–290.

[4] M. Chen, Stability analysis and Turing pattern of an enzyme-catalyzed reaction-diffusion system, *MATCH Commun. Math. Comput. Chem.* **94** (2025) 195–214.

[5] M. C. Cross, P. C. Hohenberg, Pattern formation outside of equilibrium, *Rev. Mod. Phys.* **65** (1993) 851–1112.

[6] O. Diekmann, S. van Gils, S. Verduyn Lunel, H.-O. Walther, *Delay Equations: Functional, Complex, and Nonlinear Analysis*, Springer, New York, 1995.

[7] Q. Din, Dynamics and Hopf bifurcation of a chaotic chemical reaction model, *MATCH Commun. Math. Comput. Chem.* **88** (2022) 351–369.

[8] Q. Din, U. Saeed, Stability, discretization, and bifurcation analysis for a chemical reaction system, *MATCH Commun. Math. Comput. Chem.* **90** (2023) 151–174.

[9] Q. Din, M. S. Shabbir, M. A. Khan, A cubic autocatalator chemical reaction model with limit cycle analysis and consistency preserving discretization, *MATCH Commun. Math. Comput. Chem.* **87** (2022) 441–462.

[10] T. Faria, Normal forms and Hopf bifurcation for partial differential equations with delays, *Trans. Am. Math. Soc.* **352** (2000) 2217–2238.

[11] M. Chen, Z. Hu, Q. Zheng, H. M. Srivastava, Dynamics analysis of a spatiotemporal SI model, *Alexandria Eng. J.* **74** (2023) 705–714.

[12] M. Chen, R. Wu, Patterns governed by chemotaxis and time delay, *Phys. Rev. E* **109** (2024) #014217.

[13] M. Chen, Taxis-driven complex patterns of a plankton model, *Chaos* **34** (2024) #063101.

[14] Y. Lv, Turing–Hopf bifurcation analysis and normal form in a delayed diffusive predator–prey system with taxis and fear effect, *Z. Angew. Math. Phys.* **76** (2025) #7.

[15] Q. Zheng, The consequence of the proportional–derivative controller on Turing instability in a predator–prey model, *Appl. Math. Lett.* **178** (2026) #109941.

[16] M. Chen, X.-Z. Li, C. Tian, Turing instability and complex pattern evolution of a Gierer–Meinhardt model, *Nonlin. Dyn.* **114** (2026) #535.

[17] M. Chen, X. Li, X. Z. Li, R. Wu, Turing instability of equilibrium and periodic solution for an enzyme-catalyzed system, *MATCH Commun. Math. Comput. Chem.* **95** (2026) 659–694.

[18] R. J. Field, R. M. Noyes, Oscillations in chemical systems. IV. Limit cycle behavior in a model of a real chemical reaction, *J. Chem. Phys.* **60** (1974) 1877–1884.

[19] X. Gao, Y. Jin, M. Marwan, F. Li, Y. Wei, Impact of Hopf and Bautin bifurcations on an autocatalytic chemical reaction system, *MATCH Commun. Math. Comput. Chem.* **94** (2025) 863–889.

[20] A. Gierer, H. Meinhardt, A theory of biological pattern formation, *Kybernetik* **12** (1972) 30–39.

[21] R. Golnik, P. F. Stadler, T. Gatter, Atom transition networks and isotope labeling patterns in large chemical reaction networks, *MATCH Commun. Math. Comput. Chem.* **95** (2026) 347–404.

[22] J. K. Hale, S. M. Verduyn Lunel, *Introduction to Functional Differential Equations*, Springer, New York, 1993.

[23] B. D. Hassard, N. D. Kazarinoff, Y. H. Wan, *Theory and Applications of Hopf Bifurcation*, Cambridge Univ. Press, Cambridge, 1981.

[24] M. Izadi, H. Ahmad, H. M. Srivastava, Numerical computations of time-dependent autocatalytic glycolysis reaction-diffusion system, *MATCH Commun. Math. Comput. Chem.* **93** (2025) 69–97.

[25] A. Jan, R. A. Shah, H. Ahmad, H. Bilal, B. Almohsen, Dynamic behavior of enzyme kinetics cooperative chemical reactions, *AIP Adv.* **14** (2024) #035139.

[26] A. Jan, R. A. Shah, H. Ahmad, H. Bilal, B. Almohsen, Dynamics and stability analysis of enzymatic cooperative chemical reactions in biological systems with time-delayed effects, *Part. Diff. Eq. Appl. Math.* **11** (2024) #100850.

[27] M. A. Khan, Q. Din, Codimension-one and codimension-two bifurcations of a fractional-order cubic autocatalator chemical reaction system, *MATCH Commun. Math. Comput. Chem.* **91** (2024) 415–452.

[28] M. A. Khan, Q. Din, W. Abdelfattah, Codimension-two bifurcation of a fractional-order Schnakenberg chemical reaction system, *MATCH Commun. Math. Comput. Chem.* **94** (2025) 327–354.

[29] C. Kuehn, *Multiple Time Scale Dynamics*, Springer, Cham, 2015.

[30] I. Lengyel, I. R. Epstein, Modeling of Turing structures in the chlorite–iodide–malonic acid–starch reaction system, *Science* **251** (1991) 650–652.

[31] P. K. Maini, R. E. Baker, C. M. Chuong, Developmental biology. The Turing model comes of molecular age, *Science* **314** (2006) 1397–1398.

[32] M. Mimura, J. D. Murray, On a diffusive prey-predator model which exhibits patchiness, *J. Theor. Biol.* **75** (1978) 249–262.

[33] J. D. Murray, *Mathematical Biology II: Spatial Models and Biomedical Applications*, Springer, New York, 2003.

[34] G. Nicolis, I. Prigogine, On symmetry-breaking instabilities in dissipative systems, *J. Chem. Phys.* **46** (1967) 3542–3550.

[35] G. Nicolis, I. Prigogine, *Self-Organization in Nonequilibrium Systems*, Wiley, New York, 1977.

[36] R. Peng, F. Yi, X. Zhao, Spatiotemporal patterns in a reaction-diffusion model with the Degn–Harrison reaction scheme, *J. Diff. Eq.* **254** (2013) 2465–2498.

[37] I. Prigogine, R. Lefever, Symmetry breaking instabilities in dissipative systems II, *J. Chem. Phys.* **48** (1968) 1695–1700.

[38] J. Schnakenberg, Simple chemical reaction systems with limit cycle behaviour, *J. Theor. Biol.* **81** (1979) 389–400.

[39] H. L. Smith, Oscillations and multiple steady states in a cyclic gene model, *J. Math. Biol.* **25** (1987) 169–190.

[40] A. M. Turing, The chemical basis of morphogenesis, *Philos. Trans. R. Soc. Lond. B* **237** (1952) 37–72.

[41] J. J. Tyson, Some further studies of nonlinear oscillations in chemical systems, *J. Chem. Phys.* **58** (1973) 3919–3930.

[42] J. Wei, M. Winter, *Mathematical Aspects of Pattern Formation in Biological Systems*, Springer, London, 2014.

[43] H. Wong, M. J. Ward, Spot patterns in the Schnakenberg model with localized heterogeneities, *SIAM J. Appl. Dyn. Syst.* **15** (2016) 1739–1785.

[44] J. Wu, *Theory and Applications of Partial Functional Differential Equations*, Springer, New York, 1996.

[45] R. Wu, L. Yang, Bogdanov–Takens bifurcation of an enzyme-catalyzed reaction model, *Nonlin. Dyn.* **112** (2024) 14363–14377.

[46] C. Xu, Y. Yao, Z. Liu, P. Li, L. Yao, Bifurcation caused by delay in a fractional-order coupled Oregonator model in chemistry, *MATCH Commun. Math. Comput. Chem.* **88** (2022) 371–396.

[47] F. Yi, X. Zhao, J. Wei, Turing pattern under the influence of diffusion and delay in a Schnakenberg-type model, *Nonlin. Anal. Real World Appl.* **40** (2018) 101–125.

[48] X. Zhao, Spatiotemporal oscillations of an enzyme-catalyzed model, *MATCH Commun. Math. Comput. Chem.* **94** (2025) 605–631.

[49] J. Zhou, X. Hua, Y. Chen, Y. Ye, Pattern formation in an enzyme-catalyzed reaction-diffusion system on complex networks: the coupling mechanism of topology and dynamics, *MATCH Commun. Math. Comput. Chem.* **96** (2026) 99–128.

[50] R. M. Zulqarnain, I. Ahmad, G. Ali, R. Ali, Y. Wang, M. Marwan, Fractional modeling of cooperative enzyme kinetics with neural network validation, *MATCH Commun. Math. Comput. Chem.* **96** (2026) 129–157.